

Competitive Strain Modulation of Oxygen Reduction Reaction in Monolayer Binary Alloy Surfaces

Mailde S. Ozório^[a], Marcus F. Nygaard,^[a] Jan Rossmeisl^[a]

^[a] Center for High Entropy Alloy Catalysis (CHEAC), Department of Chemistry, University of Copenhagen, Universitetsparken 5, DK-2100 Copenhagen, Denmark, E-mail: mdso@chem.ku.dk, jan.rossmeisl@chem.ku.dk

Abstract

Binary alloys of transition metals are promising catalytic materials for the cathodic oxygen-reduction reaction (ORR) of polymer-electrolyte-membrane fuel cells (PEMFCs). However, a lack of understanding of the factors that affect the ORR's catalytic performance hampers the catalytic applications of binary alloys. To obtain further knowledge of binary alloys for efficient ORR, we investigate the activity of monolayer $\text{Au}_x\text{Pt}_{1-x}$ alloy surfaces supported on Pt(111), considering from random distribution until phase-segregated surface atoms. Using the ${}^*\text{OH}$ adsorption energy as a descriptor, we found that the activity of monolayer binary alloy surfaces depends on the distribution of the surface atoms within surfaces with segregated Pt and Au domains showing higher activity. The adsorption energy of ${}^*\text{OH}$ increases with the fraction n of Au near the adsorption site and decreases with the fraction p of Au outside the heptamer. The energy increase due to n is related to a tensile strain, while the decrease with the increase of p is due to a long-range surface strain effect on the Pt-Pt and Pt-Au bonds, improving the activity of the available Pt adsorption sites. Due to the weak ${}^*\text{OH}$ adsorption energy on Au sites, an Au overall percentage considerably above the Pt percentage starts to reduce surface activity because of the reduction of the number of very active Pt sites.

Key-words: Platinum gold alloys, Oxygen reduction reaction, Long-range surface strain

Introduction

Polymer-electrolyte-membrane fuel cells (PEMFCs) are potential power sources to reduce fossil fuel consumption, and applications may include portable technologies and transportation.¹ In PEMFCs cathode, the oxygen reduction reaction (ORR) is a limiting step that takes place through the formation of ${}^*\text{O}$, ${}^*\text{OH}$, and ${}^*\text{OOH}$ intermediates during the formation of water from the half-cell reduction of O_2 molecules ($\text{O}_2 + 4\text{H}^+ + 4\text{e}^- \rightarrow 2\text{H}_2\text{O}$).^{2,3} Various mono-metallic catalysts have been considered to improve the efficiency of ORR to resolve the sluggish cathodic kinetics.^{4–6} The most common commercial catalyst for ORR is Pt/C, which facilitates the four-electron mechanism of ORR at high potential with a low energy barrier.⁷ However, the high loading of Pt increases the catalyst cost and requires the design of cheaper catalysts with enhanced stability and activity under *operando* conditions.⁸ Consequently, further research at the atomic level is needed to design catalysts for the ORR that overreach the mainstream carbon-supported Pt catalyst (Pt/C).

To reduce the Pt loading, the spotlight has been on developing alternative catalysts with minimal or no Pt content through Pt alloying with more abundant or less expensive elements, and much progress has been made in this aspect.^{8–16} In particular, Pt-Au alloys have potential use as catalysts for ORR. The enhanced performance of the Pt-Au core-shell electrocatalyst has been attributed to the shortened Pt-Pt bond lengths of the surface induced by the core.^{17,18} Various types of Pt-Au alloys, such as platinum-gold monolayer, core-shell structures, and nanocomposite, have shown that gold can improve the stability of the catalyst.^{13,19–21} Towards the ORR, adding Au clusters to the Pt nanocatalysts has also demonstrated a practical approach to stabilizing Pt nanoparticle catalysts by avoiding Pt dissolution.^{22,23}

Regarding the Pt and Au surfaces, different behaviors exist concerning the adsorption energy of ORR intermediates. For instance, the Pt(111) surface binds the *OH intermediate stronger than the optimal catalyst, and the Au(111) surface binds it too weakly.^{3,24} The weak adsorption energy of ORR intermediates on the Au surface has been attributed to a repulsive coupling between the ORR adsorbates and the *d* orbitals of Au.²⁵ When mixing those metals, although Pt-Au solid solution has been identified for nanocatalysts depending on the applied methodology, the phase diagram miscibility gap between Pt and Au indicates higher odds of phase separation, making obtaining the solid bulk solution challenging.^{26–28} Previous research reveals the surface Au and Pt segregation tendency,^{29–31} and the likelihood of finding Au at the surface/near-surface than in the deep layers.^{32–36} And more recently, a long-range surface strain on gold was discovered on stepped Pt surfaces,²¹ which suggests that despite Au nobility towards participating in the ORR kinetics, their significantly larger lattice parameter could make the Pt sites better catalytic sites than the bare Pt(111), analogous to the observed for the Ag_xPt_{1-x}/Pt(111) surfaces.¹² Consequently, further investigating Pt-Au alloys on the surface/near-surface could provide crucial information for designing new catalysts.

Here, the focus is to provide a better understanding of the effects of a monolayer Pt-Au alloying on Pt(111) substrate. To achieve this, we conducted a comprehensive theoretical investigation of the ORR activity trends of monolayer binary Au_xPt_{1-x}/Pt(111) surfaces, where the amount of gold in the topmost surface was increased from 0 to 100%. Using the *OH adsorption energy as a descriptor, we predicted the activity of extended surfaces from 0 to 89% of Au composition. Those surfaces align with the counting of the fcc trimers as determined by early experimental scanning tunneling microscopy (STM),³⁰ which suggests a slight phase-segregation likelihood of Pt and Au at the surface. To predict the activities, noting that the distribution of Au and Pt surface atoms might affect the catalytic performance of monolayer Au_xPt_{1-x}/Pt(111) surfaces, we also considered different surface atoms arrangements, i.e., random distribution and well-defined Au-rich and Pt-rich domains.

We found the activity performance of monolayer binary alloy surfaces is directly influenced by the different arrangements of surface atoms, which, the competitive interplay between long-range surface strain and tensile strain plays a pivotal role in determining the activity contribution of varying adsorption sites. Since the same surface composition can represent a myriad of surface atom distributions, these results indicate that controlling the distribution of surface atoms is crucial to ensure the reproducibility of a catalyst's performance. Avoiding generalized conclusions based on a single observation can provide

robust information for designing new catalysts with improved performance and lifespan. Henceforth, our results are presented and discussed in detail.

Methodology

Aiming for a better understanding of the atomistic effects behind the monolayer $\text{Au}_x\text{Pt}_{1-x}/\text{Pt}(111)$ surfaces, using version 22.8.0 of GPAW³⁷, we carried out density-functional theory (DFT) calculations of the *OH binding on different $\text{Au}_x\text{Pt}_{1-x}/\text{Pt}(111)$ surfaces by considering 4x4x4 and 5x5x4 slabs, by increasing the amount of Au from 0% to 100%. We thought the adsorption of *OH on on-top sites of Pt and Au with different neighboring atoms, i.e., the $\text{Pt}(\text{Au}_y\text{Pt}_{6-y})$ and $\text{Au}(\text{Au}_y\text{Pt}_{6-y})$ ($0 \leq y \leq 6$). The interaction between the valence electrons and the ion cores was described by the projector-augmented wave (PAW)³⁸ method, as implemented in GPAW. The DFT calculations were performed considering the plane-augmented wave method (PAW)³⁸ and the atomic-scale environment (ASE).³⁹ The exchange-correlation interactions were treated within the RPBE⁴⁰ functional.

The $\text{Au}_x\text{Pt}_{1-x}/\text{Pt}(111)$ surfaces were modeled using a periodic slab approach with 4x4x4 and 5x5x4 sizes, ensuring sufficient vacuum space of 10 Å along the z-axis to avoid spurious interactions. We employed the same convergence criterion for all the surface calculations, i.e., Brillouin zone integrations were carried out using a Monkhorst-Pack grid of 4x4x1 k-points mesh. To mimic the slab's bulk-like Pt(111) substrate behavior and reduce the computational cost, the two bottom layers of the slab were fixed at their Pt bulk positions. In contrast, the remaining top layers were allowed to relax until the forces on the atoms were equal to or less than 0.1 eV Å⁻¹. An energy cutoff of 400 eV was used for the plane-wave basis set.

To predict the ORR activity, we utilized the universal scaling relation, which establishes a linear relationship between the adsorption energies of *OH and *OOH intermediates. This relationship is defined as $\Delta E_{*OOH} = \Delta E_{*OH} + 3.2 \text{ eV}$.^{41 42 43} This scaling relation is advantageous because both *OH and *OOH intermediates adsorb on top sites, indicating that a single ORR descriptor (either the *OH or *OOH binding energy) can predict the ORR activity of both heterometallic and monometallic surfaces.^{44,45} Conversely, since *O intermediates adsorb on fcc sites, the *O/*OH scaling relation does not apply to heterometallic surfaces. Therefore, instead of using the *O adsorption energy as a descriptor,⁴⁶ we employed the *OH binding energy to predict the ORR activity of $\text{Au}_x\text{Pt}_{1-x}/\text{Pt}(111)$ surfaces. As we did in our previous work,¹² the ORR activity was calculated using the following equation:

$$j_{k_i} = Ae^{\frac{(-|\Delta E_i - \Delta E_{opt}| + 0.86eV - eU)}{K_B T}},$$

Where eU stands for the applied potential, T is the room temperature, ΔE_i is the *OH adsorption energy, and ΔE_{opt} is 0.1 eV, which corresponds to the difference in the binding energy of the ideal catalyst and Pt.⁴⁷ A is a constant, which the value of 0.5 u.a was

considered. This approach leverages the consistency and reliability of the ${}^*\text{OH}$ binding energy as a predictive descriptor for ORR activity in the studied surfaces.

Results and Discussion

In considering the ${}^*\text{OH}$ adsorption energy as a descriptor for the ORR on $\text{Au}_x\text{Pt}_{1-x}/\text{Pt}(111)$ surfaces, there exists a large variety of configurations for each gold as on-top sites as well as Pt as on-top sites. However, the performance of each site depends on how strongly the ${}^*\text{OH}$ interacts with the surface, i.e., as stated by the Sabatier principle, the interaction cannot be too strong nor too weak.⁴⁸ In particular, in considering the optimal adsorption of ${}^*\text{OH}$ in 0.1 eV,² the Au sites are irrelevant ORR catalytic on-top sites because the ${}^*\text{OH}$ adsorption energy is too weak on Au (> 0.6 eV, see Fig S1). On the other hand, the ${}^*\text{OH}$ adsorption energy on on-top Pt sites is closer to the optimal, within most of the ${}^*\text{OH}$ adsorption on $\text{Pt}(\text{Au}_y\text{Pt}_{6-y})$ heptamers in the 0.0 - 0.1 eV range, where $(\text{Au}_y\text{Pt}_{6-y})$ ($0 \leq y \leq 6$) represents the six nearest surface atoms to the Pt adsorption site. Consequently, as observed for the monolayer $\text{Ag}_x\text{Pt}_{1-x}/\text{Pt}(111)$ surfaces,¹² only the Pt sites can speed up the cathodic ORR rates. The energy difference of similar heptamers is unrelated to ensemble effects since all the ${}^*\text{OH}$ intermediate adsorb on on-top Pt sites. Nevertheless, once the ${}^*\text{OH}/\text{Pt}(\text{Au}_y\text{Pt}_{6-y})$ sites have all the potential to improve the ORR performance of $\text{Au}_x\text{Pt}_{1-x}/\text{Pt}(111)$ surfaces compared to that of $\text{Pt}(111)$, then we further investigated what physical-chemistry effects make them comparable with $\text{Pt}(111)$.

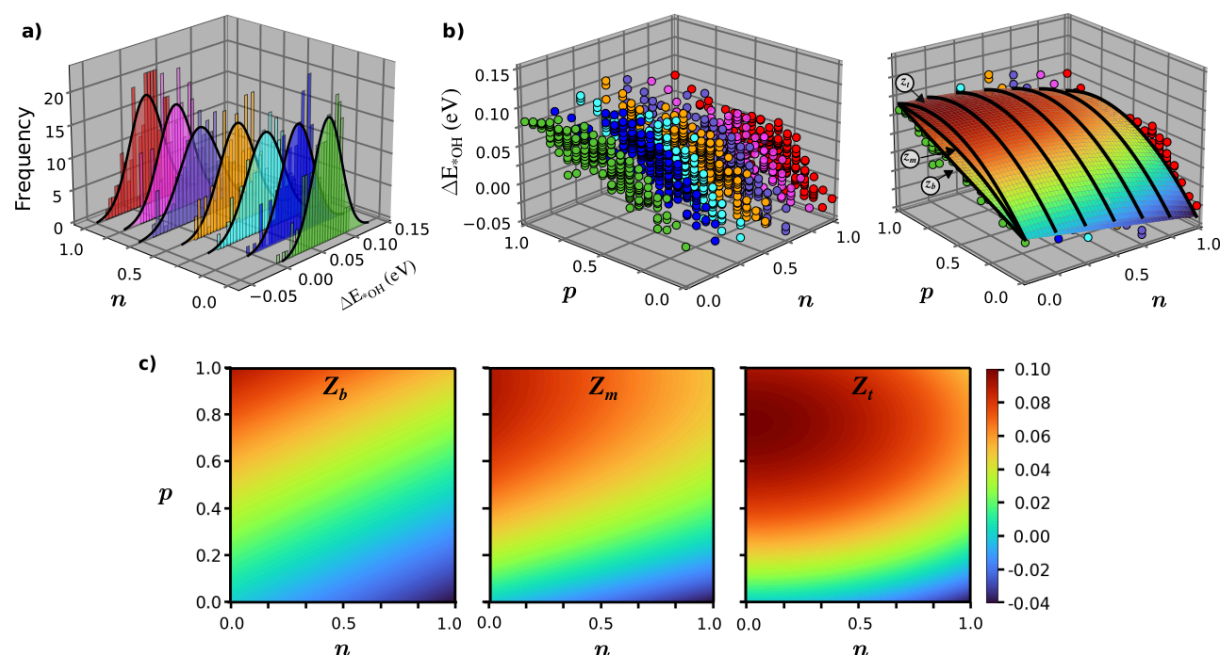


Figure 1. **a)** The ${}^*\text{OH}$ adsorption energy distribution on on-top Pt sites of $\text{Au}_x\text{Pt}_{1-x}/\text{Pt}(111)$ surfaces as a function of the fraction n of Au atoms in the ring $(\text{Au}_y\text{Pt}_{6-y})$ ($0 \leq y \leq 6$) neighboring the Pt adsorption site, i.e., $\text{Pt}(\text{Au}_y\text{Pt}_{6-y})$ ($0 \leq n = y/6 \leq 1$). **b)** The ${}^*\text{OH}$ binding energy as a function of n and the fraction p of Au outside the heptamer. The plot on the left illustrates three surfaces in which geodesic curves approach the strongest (z_b plane), average (z_m surface), and weakest (z_t surface) ${}^*\text{OH}$ adsorption energy for each (p, n) . In an

electronvolt (eV) unit, the equations are $z_b = 0.09p - 0.04n$, $z_m = -0.10p^2 + 0.19p - 0.04n$, and $z_t = -0.17p^2 + 0.26p - 0.04n^2$. **c)** Projection of the *OH adsorption energy in the pn plane, which reveals the activity of Pt adsorption sites mostly approaches the optimal as n decreases and p increases.

The geodesic curves of the surfaces depicted in Figure 1 were considered to predict the activity of the binary surfaces by evaluating the weakest *OH adsorption energy (z_t), the strongest *OH adsorption energy (z_b), and, since the *OH adsorption energy ranges in the interval of $z_t \leq \Delta E_{*OH} \leq z_b$, we also considered an average *OH adsorption energy described by $\Delta E_{*OH} = z_m$ surface. Considering this energy range, we can obtain different continuous ΔE_{*OH} functions for each $\text{Pt}(\text{Au}_y\text{Pt}_{6-y})$ ($0 \leq y \leq 6$) heptamer. This approach helps overcome the limitation of calculating a myriad of combinatory possibilities for the Au/Pt distributions at the surface. The *OH adsorption energy relies solely on only two variables: the fraction p of Au outside and the fraction n of Au inside the heptamer. For the clean Pt(111) reference, all $\text{Pt}(\text{Pt}_6)$ heptamers are equivalents, i.e., within the reference *OH adsorption energy of 0.00 eV. However, the left panel of Figure 1b shows that the *OH adsorption energy on on-top Pt of $\text{Pt}(\text{Pt}_6)$ heptamers ranges between 0.00 eV and 0.09 eV. in the inhomogeneous surfaces due to changes in the fraction p of Au outside the heptamer.

It is well-known that H_2O_2 formation is favored at very negative potentials through the two-electron mechanism,^{49–52} while the four-electron mechanism towards the formation of H_2O is favored at a more positive potential (low overpotentials).³ Here, we are interested in exploring the activity of binary surfaces toward the four-electron mechanisms, the reason why we focus on the low overpotential regions, and by considering the *OH adsorption energy (z_b , z_m , and z_t) of the Pt active sites as a descriptor to predict the activity of extended $\text{Au}_x\text{Pt}_{1-x}/\text{Pt}(111)$ surfaces. As shown in Figure 2a, we considered extended surfaces with compositions from 0 - 89% of Au and within different distributions of Au and Pt surface atoms, i.e., random distribution (I), slight phase separation (II), and with more well-defined Au-rich and Pt-rich domains (III).

It should be mentioned that the surfaces shown in Figure 2a (II) up to 51% of Au (highlighted inside a blue rectangle) exhibit an excellent agreement with the experimental counting of the fcc Au_3 , Au_2Pt , AuPt_2 , and Au_3 trimers, as determined by atomic-scale resolution scanning tunneling microscopy (STM) analysis.³⁰ These STM-based $\text{Au}_x\text{Pt}_{1-x}/\text{Pt}(111)$ surfaces were obtained with our previous model based on an adjustable cutoff radius.¹² The model's ability to accurately reproduce the experimental STM atomic distribution has also been evidenced in our previous work on $\text{Ag}_x\text{Pt}_{1-x}/\text{Pt}(111)$ surfaces.¹² Also, it is used to generate random, partial phase-separation, and complete phase-segregation distributions of the atoms by adjusting the cutoff radius.

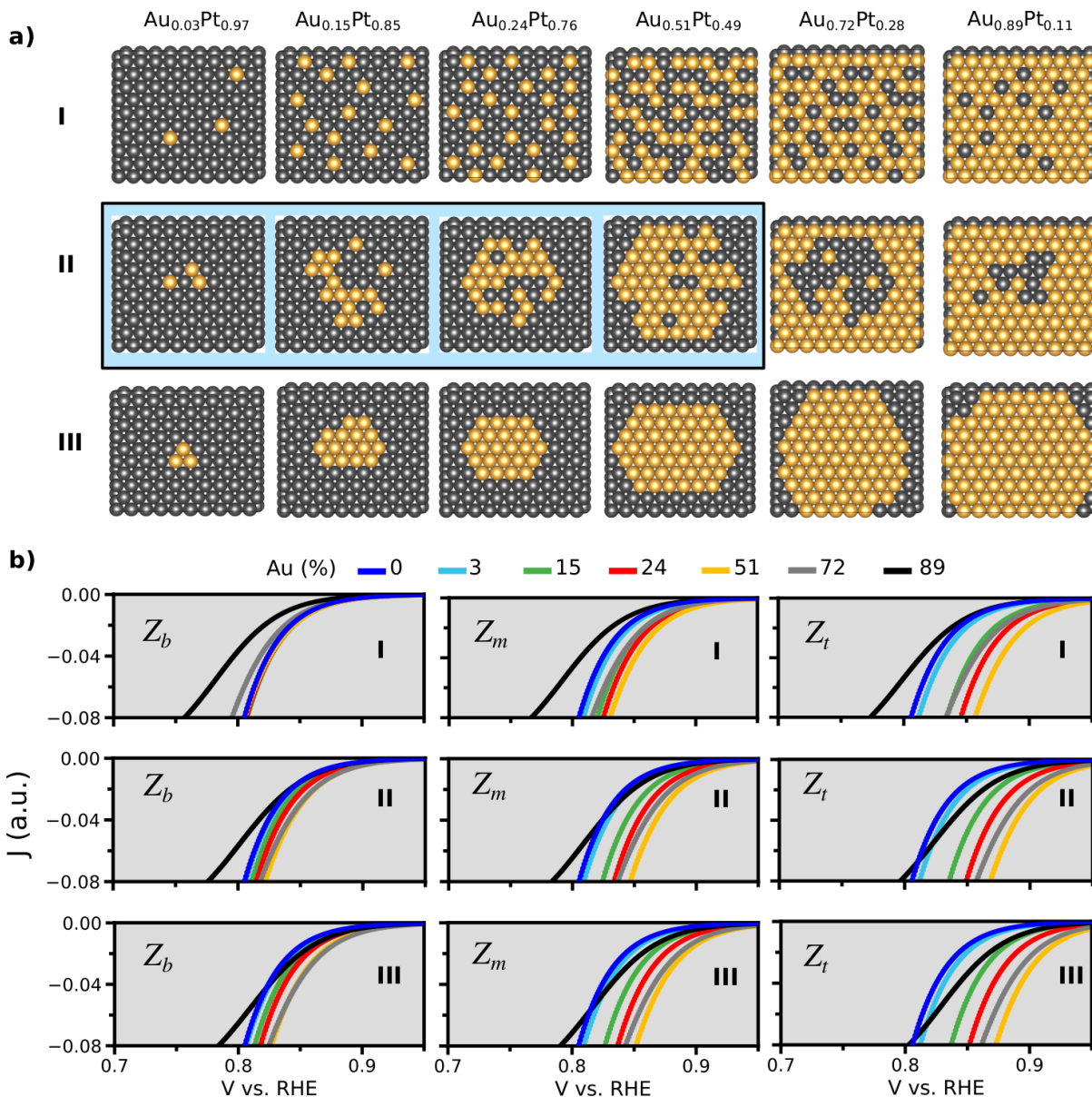


Figure 2 a) (I) Random distribution, no-phase separation (II) Slight phase-separation Au_xPt_{1-x}/Pt(111) surface configurations, which surfaces highlighted in the blue area are in line with STM analysis, e.g., for the Au_{0.51}Pt_{0.49}/Pt(111) surface the Au and Pt exactly satisfy the experimental fcc Au₃, Au₂Pt, AuPt₂, and Au₃ trimers counting of 28%, 23%, 23%, and 28%, respectively.³⁰ See the support information for additional details about the trimer countings of the Au_xPt_{1-x}/Pt(111) surfaces. (III) Phase-segregated Au_xPt_{1-x}/Pt(111) representative surface configurations. The Pt atoms are represented in dark grey, while the Au atoms are in yellow in the 10x10 surface atoms. **b)** Polarization curves of (I), (II), and (III) surfaces by considering z_b , z_m , and z_t *OH adsorption energy as a descriptor.

Figure 2b shows the simulated polarization curves for the three representative sets of random (I), slight phase-separation (II), and phase-segregated extended Au_xPt_{1-x}/Pt(111) surfaces (III). The values of z_b as descriptors for the *OH adsorption energy show that the activity of binary alloy surfaces with Pt loading higher than 20% is considerably better or comparable to Pt(111), where the activity of each Pt(Au_yPt_{6-y}) ($0 \leq n = y/6 \leq 1$) heptamer is improved compared to Pt(Pt₆) of Pt(111) when p is higher than $\sim 0.45n$. Increasing n requires a larger fraction p of Au outside the heptamer to provide the same activity as

Pt(111). It is also observed for the weak *OH adsorption energies described by z_m and z_t , for what the net effect of p -terms ($0 < p \leq 1$) is making the *OH adsorption energy weaker, while the net effect of n -terms ($0 < n \leq 1$) is making the *OH adsorption energy stronger.

A general observation consists of enhancing the binary surface activity compared to Pt(111) as the Au and Pt distributions move towards more defined Pt and Au separations, i.e., independent of the descriptor (column trends of Figure 2b), the binary surface activity improves in the sequence I → II → III of the surface atoms arrangement. The opposite behavior between p and n explains why the activity of surfaces increases in the sequence of I → II → III, i.e., moving towards this sequence, the number of Pt(Au_yPt_{6-y}) heptamers with few Au atoms increase (reducing the overall effect of n), and the fraction p increase, which contributes for weaker *OH adsorption. Since the bottom Au_xPt_{1-x}/Pt(111) surfaces are all Pt sites, this underscores the pivotal role of surface atom arrangements in the activity, i.e., in addition to the well-known surface composition effect,^{53,54} different distributions of surface atoms imply significant changes in the catalytic performance for identical surface composition. Yet, the atom distributions have also been shown to affect catalysts with different architectures, e.g., Pt-skin and Pt-skeleton catalysts with alloyed subsurface were found to have different catalytic properties of pure polycrystalline Pt because of the different arrangements of the subsurface atoms.⁵⁵ As a consequence, for the reproducibility of catalyst performance, in addition to the control of the catalyst shape-size-composition triad,^{56–61} these results reflect the need to overcome the challenge of controlling the arrangements of the atoms in alloyed catalyst, engaging further research in this area.

Based on experimental cyclic voltammograms, binary Au_xPt_{1-x}/Pt(111) surface alloy polarization curves have similarities with Pt(111) for the amount of Au until 24%; increasing the content of Gold (above 51%) is observed the activity decrease.³⁰ These observations align with our simulated polarization curves of experimental-based surfaces predicted with z_b (highlighted in blue in Figure 2a). However, we not only find nearly Pt(111) activity until 24% of Au but also surface with an amount of Au as high as 72%. A considerable increase in Au decreases the activity (see Figure S3). Based on that, it is worth noting that some Pt sites may be unavailable under real conditions, affecting the simulated trends, as the simulations consider all Pt sites active to adsorb *OH and no ORR-interfering phenomena. Even though surface Au atoms can decrease Pt dissolution,^{22,62,63} since surfaces with more than 50% Au have few Pt sites available, the unavailability of some Pt sites of Au-rich Au_xPt_{1-x}/Pt(111) surfaces can significantly reduce their activity.

Since this opposite behavior of Au outside and inside the heptamer determines the activity of the binary surface, we analyzed it in more detail. The architecture of the Au_xPt_{1-x}/Pt(111) surfaces is such that the Pt(111) substrate determines the overall lattice parameter of the unit cell.³⁰ Consequently, as confirmed for Ag_xPt_{1-x}/Pt(111) surfaces,¹² the self-induced long-range surface strain of Pt-Pt(Au) bonds on the surface monolayer might affect the *OH adsorption energy on Au_xPt_{1-x}/Pt(111). This is due to the Au and Pt lattice parameters mismatch, respectively, 4.065 Å and 3.912 Å.⁶⁴ To confirm the strain effect in the Au_xPt_{1-x}/Pt(111) surfaces, the *OH binding energy on different Pt(Au_yPt_{6-y}) heptamers are plotted in the left panel of Figure 2 (a) as a function of the variation of the area of the Pt adsorption site relative to Pt(111). It is observed a weakening of the *OH adsorption energy within the area contraction, which is related to the increase of Au outside the heptamer,

which confirms a long-range compressive strain yielded by Au, causing the Pt-Pt and Pt-Au bonds to be shortened. This can be straightforwardly observed from the area decrease of Pt(Pt₆) of Pt(Au₆) heptamers, in which the central atoms form only Pt-Pt and Pt-Au bonds with their following neighboring atoms. In line with our findings, a long-range strain field was demonstrated to be caused by Au deposition or surface defects.²¹

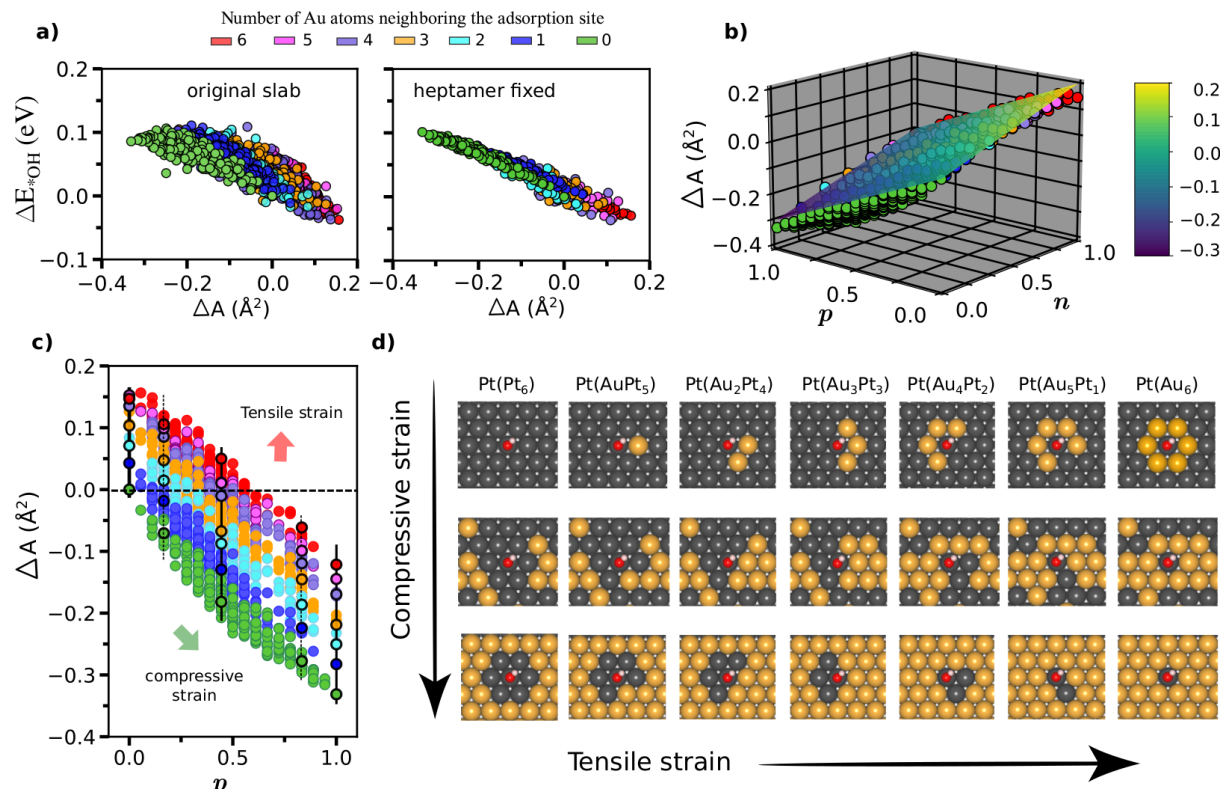


Figure 2. **a)** The *OH adsorption energy is shown as a function of the area compression of the adsorption site considering *i*) the original slabs (up panel) and *ii*) the heptamer features of original slabs fixed (same atom's position and composition) within replacing all the Au outside from the heptamer with Pt. The area corresponds to the hexagon with vertices in the middle distance between the Pt adsorption site and the six neighboring (Au,Pt_{6-y}) ($0 \leq y \leq 6$) atoms. **b)** The area compression satisfies the plane equation: $\Delta A = -0.30p + 0.20n$. For simplicity, **c)** following the vertical lines along the direction of the red arrow, compared to the Pt(Pt₆) with similar Au surface composition and atomic distribution, all other Pt(Au_{6-y}) ($y > 0$) heptamers face a gradation area expansion (tensile strain) due to the increase of Au. In contrast, in the direction of the green arrow, all heptamers suffer a self-induced long-range strain due to increased Au on the surface. **d)** Representation of the surfaces along the filled vertical lines of Figure 2(a) with their respective *OH adsorption energy relative to Pt(111). The first and last rows show none and maximal self-induced long-range surface strain effects on the heptamers; the middle row is in between.

Again, we simulated all the binary surface calculations to get additional evidence of the strain effect in the *OH adsorption energy. We now fix the heptamers' atomic positions and compositional features while replacing all the Au atoms apart from the heptamer with Pt. Keeping the position of the atoms fixed, we keep the longe-range compressive strain field induced by the farthest Au atoms. The results are plotted in Figure 2(b). The *strained* heptamers have similar *OH adsorption energy trends as the binary surface without replacing Au apart from the heptamer, i.e., despite structural-electronic contributions apart from the heptamer existing, they are not higher in magnitude than the effects that come from the *strained* heptamers.

Figure 2c reveals a correlation between the adsorption site's hexagonal area and the fraction p of Au outside the heptamer, i.e., the area decreases almost perfectly linearly with increasing Au content apart from the heptamer, the Pt-Pt and Pt-Au of all $\text{Pt}(\text{Au}_y\text{Pt}_{6-y})$ heptamers are larger for 0% of Au and suffer the highest compression when 100% of surface atoms apart from the heptamer is Au ($\Delta A = -0.30p + 0.20n$). Conversely, the increase of Au inside the heptamer increases the tensile strain. The effect of tensile strain can be observed when the structural composition apart from the heptamer is the same, and the heptamer Au composition is increased from $\text{Pt}(\text{Pt}_6) \rightarrow \text{Pt}(\text{Ag}_6)$. This is shown in Figure 2(c) through the vertical lines, in which each line represents surfaces differentiating only in the Au content in the heptamer. At this point, we can name the opposite p and n effects. The long-range surface strain is behind the weakening of the binding energy with the increasing fraction p of Au outside the heptamer, while n is doing the opposite; it is a tensile strain making the *OH binding energy stronger.

To illustrate the effect of the comprehensive and tensile strain, we highlight the surfaces corresponding to the filled vertical lines of Figure 2(c) in Figure 2(d). Each column evidences the long-range compressive surface strain on the heptamer, which weakens the *OH binding energy by increasing the Au content. Along each row, since the surface composition apart of the heptamer is similar, the significant role in the *OH adsorption energy arises mainly from the heptamer change, where the net physical-chemistry effect results in a tensile strain, which is behind the slight decrease of *OH adsorption energy when increasing the Au content in the heptamer. Consequently, the heptamers richer in Au, i.e., $\text{Pt}(\text{Au}_y\text{Pt}_{6-y})$ $y > 3$, suffer more internal effects. Undoubtedly, the tensile strain is weaker in magnitude compared to the long-range compressive strain, with this later making the *OH adsorption energy on $\text{Pt}(\text{Ag}_6)$ approach the optimal value of 0.1 eV when 100% of Au apart of the heptamer are Au.

Increasing the Au neighbors, an area expansion around the Pt adsorption site exists because, on average, the Pt-Au bonds range between the Pt-Pt bonds of $\text{Pt}(111)$ (2.766 Å) and the Au-Au bonds of $\text{Au}(111)$ (2.874 Å).⁶⁴ However, this feature is not the only source of the tensile strain observed with increased Au around the adsorption. This can be shown by the difference in the area occupied by the Pt adsorption site in the $\text{Pt}(\text{Au}_y\text{Pt}_{6-y})$ heptamers with and without the *OH adsorbed. As shown in Figure 3a, there exists an upshift of the $\text{Pt}(\text{Au}_y\text{Pt}_{6-y})$ heptamers area for the *OH/ $\text{Pt}(\text{Au}_y\text{Pt}_{6-y})$, which are all higher than the respective heptamer with no adsorbates (see Figure 3b). These results suggest an increase of tensile strain yielded by stronger interactions of the electronic states of *OH and the d states of Pt/Au elements. Increasing Au increases the hybridization of *OH orbitals and the d-states of Pt and Au, making the adsorbing stronger. However, since tensile and compressive strains compete for a restricted surface area, the increase of Au outside the heptamer will force the compression of the heptamer area.

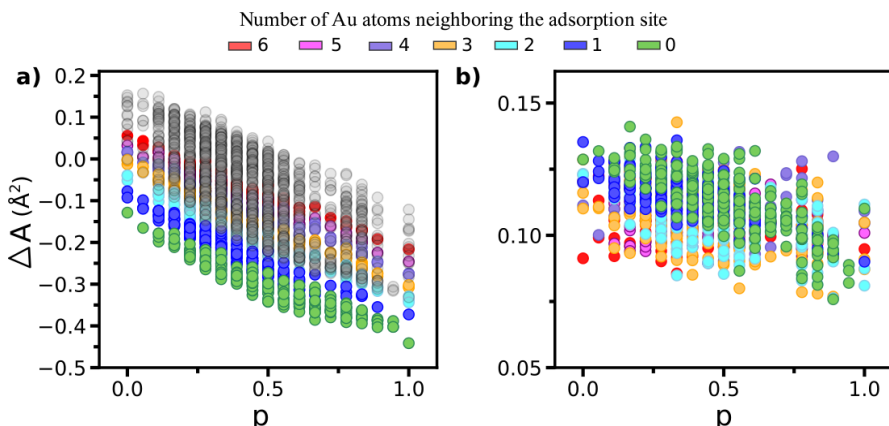


Figure 3. a) Area of the Pt(Au_yPt_{6-y}) heptamer in the absence of the *OH adsorbates highlighted from green to red according to the number of Au atoms around the Pt adsorption site. The respective heptamer area (as shown in Figure 2c) is represented again without color distinction to illustrate the upshift of the adsorption site environment due to the OH adsorption. The values are all given to the *OH/Pt(Pt₆) of the Pt(111) surface. b) The area gain due to the *OH adsorption is positive and ranges between 0.05 to 0.15 Å².

For Pt(M_yPt_{6-y}) heptamers, where M is a metal with a larger lattice parameter than Pt, the magnitude of competitive behavior of tensile and compressive strain can differ from the PtAu systems, e.g., for Pt(Ag_yPt_{6-y}) the net short-range tensile strain makes the *OH binding energy so strong that all Pt(Ag_yPt_{6-y}) with $y > 2$ are all inactive sites for ORR, where the *OH adsorbs too strong avoiding further ORR steps.¹² For comparison, the *OH adsorption energy distribution on Pt(Ag_yPt_{6-y}) is shown in Figure S4. Overall, the tensile strain strengthens the *OH binding energy on Pt, while the long-range compressive strain does the opposite.

Conclusions

This work provides valuable insights into the oxygen reduction reaction (ORR) activity of extended surfaces by considering the *OH intermediate adsorption energy as a descriptor, which was expressed as a function of two variables, i.e., the fraction n of Au inside the heptamer and the fraction p of Au outside the heptamer. Increasing the fraction p of Au outside the heptamer significantly weakens the *OH adsorption energy, while increasing the number of Au inside the heptamer has the opposite effect. Related to the increase of Au outside the heptamer, we identified a long-range surface strain induced by Au, which plays a crucial role in improving the activity of Pt sites by inducing the Pt-Pt bonds to be shorter than on the Pt(111) surface. The competitive interplay between long-range compressive and tensile surface strains is pivotal in determining the activity contribution of varying adsorption sites. Due to the strain, increasing gold can improve the activity of Au-rich surfaces until it matches or surpasses that of the Pt(111) surface.

Moreover, the ORR performance of monolayer binary alloy surfaces is directly influenced by the different arrangements of surface atoms (e.g., if the surface atoms are randomly distributed or forming Pt-rich and Au-rich domains) because those parameters affect the counting of relevant Pt active sites. These results imply that controlling the surface composition is crucial to ensure the reproducibility of a catalyst's performance. Avoiding

making general conclusions based on a single surface configuration is also essential to provide reliable information for designing new catalysts with improved performance and lifespan.

Acknowledgments

The authors acknowledge support from the Danish National Research Foundation Center for High-Entropy Alloy Catalysis (CHEAC) DNRF-149.

References

- (1) Wee, J.-H. Applications of Proton Exchange Membrane Fuel Cell Systems. *Renew. Sustain. Energy Rev.* **2007**, *11* (8), 1720–1738. <https://doi.org/10.1016/j.rser.2006.01.005>.
- (2) Stephens, I. E. L.; Bondarenko, A. S.; Grønbjerg, U.; Rossmeisl, J.; Chorkendorff, I. Understanding the Electrocatalysis of Oxygen Reduction on Platinum and Its Alloys. *Energy Environ. Sci.* **2012**, *5* (5), 6744. <https://doi.org/10.1039/c2ee03590a>.
- (3) Nørskov, J. K.; Rossmeisl, J.; Logadottir, A.; Lindqvist, L.; Kitchin, J. R.; Bligaard, T.; Jónsson, H. Origin of the Overpotential for Oxygen Reduction at a Fuel-Cell Cathode. *J. Phys. Chem. B* **2004**, *108* (46), 17886–17892. <https://doi.org/10.1021/jp047349j>.
- (4) Kondo, S.; Nakamura, M.; Maki, N.; Hoshi, N. Active Sites for the Oxygen Reduction Reaction on the Low and High Index Planes of Palladium. *J. Phys. Chem. C* **2009**, *113* (29), 12625–12628. <https://doi.org/10.1021/jp904278b>.
- (5) Lopes, P. P.; Strmcnik, D.; Jirkovsky, J. S.; Connell, J. G.; Stamenkovic, V.; Markovic, N. Double Layer Effects in Electrocatalysis: The Oxygen Reduction Reaction and Ethanol Oxidation Reaction on Au(1 1 1), Pt(1 1 1) and Ir(1 1 1) in Alkaline Media Containing Na and Li Cations. *Catal. Today* **2016**, *262*, 41–47. <https://doi.org/10.1016/j.cattod.2015.09.010>.
- (6) Mittermeier, T.; Weiß, A.; Gasteiger, H. A.; Hasché, F. Monometallic Palladium for Oxygen Reduction in PEM Fuel Cells: Particle-Size Effect, Reaction Mechanism, and Voltage Cycling Stability. *J. Electrochem. Soc.* **2017**, *164* (12), F1081–F1089. <https://doi.org/10.1149/2.0561712jes>.
- (7) Xu, S.; Kim, Y.; Park, J.; Higgins, D.; Shen, S.-J.; Schindler, P.; Thian, D.; Provine, J.; Torgersen, J.; Graf, T.; Schladt, T. D.; Orazov, M.; Liu, B. H.; Jaramillo, T. F.; Prinz, F. B. Extending the Limits of Pt/C Catalysts with Passivation-Gas-Incorporated Atomic Layer Deposition. *Nat. Catal.* **2018**, *1* (8), 624–630. <https://doi.org/10.1038/s41929-018-0118-1>.
- (8) Escudero-Escribano, M.; Verdaguera-Casadevall, A.; Malacrida, P.; Grønbjerg, U.; Knudsen, B. P.; Jepsen, A. K.; Rossmeisl, J.; Stephens, I. E. L.; Chorkendorff, I. Pt₅Gd as a Highly Active and Stable Catalyst for Oxygen Electrocatalysis. *J. Am. Chem. Soc.* **2012**, *134* (40), 16476–16479. <https://doi.org/10.1021/ja306348d>.
- (9) Huang, L.; Wei, M.; Qi, R.; Dong, C.-L.; Dang, D.; Yang, C.-C.; Xia, C.; Chen, C.; Zaman, S.; Li, F.-M.; You, B.; Xia, B. Y. An Integrated Platinum-Nanocarbon Electrocatalyst for Efficient Oxygen Reduction. *Nat. Commun.* **2022**, *13* (1), 6703. <https://doi.org/10.1038/s41467-022-34444-w>.
- (10) Zhang, J.; Vukmirovic, M. B.; Xu, Y.; Mavrikakis, M.; Adzic, R. R. Controlling the Catalytic Activity of Platinum-Monolayer Electrocatalysts for Oxygen Reduction with Different Substrates. *Angew. Chem. Int. Ed.* **2005**, *44* (14), 2132–2135. <https://doi.org/10.1002/anie.200462335>.
- (11) Beckord, S.; Brimaud, S.; Behm, R. J. The Performance of Structurally Well-Defined Ag_xPt_{1-x}/Pt(111) Surface Alloys in the Oxygen Reduction Reaction – An Atomic-Scale

- Picture. *J. Electroanal. Chem.* **2018**, *819*, 401–409.
<https://doi.org/10.1016/j.jelechem.2017.11.038>.
- (12) Ozório, M. S.; Nygaard, M. F.; Petersen, A. S.; Behm, R. J.; Rossmeisl, J. Self-Induced Long-Range Surface Strain Improves Oxygen Reduction Reaction. *J. Catal.* **2024**, *433*, 115484. <https://doi.org/10.1016/j.jcat.2024.115484>.
- (13) Gong, K.; Su, D.; Adzic, R. R. Platinum-Monolayer Shell on AuNi_{0.5} Fe Nanoparticle Core Electrocatalyst with High Activity and Stability for the Oxygen Reduction Reaction. *J. Am. Chem. Soc.* **2010**, *132* (41), 14364–14366. <https://doi.org/10.1021/ja1063873>.
- (14) Kuttiyiel, K. A.; Sasaki, K.; Choi, Y.; Su, D.; Liu, P.; Adzic, R. R. Nitride Stabilized PtNi Core–Shell Nanocatalyst for High Oxygen Reduction Activity. *Nano Lett.* **2012**, *12* (12), 6266–6271. <https://doi.org/10.1021/nl303362s>.
- (15) Chen, C.; Kang, Y.; Huo, Z.; Zhu, Z.; Huang, W.; Xin, H. L.; Snyder, J. D.; Li, D.; Herron, J. A.; Mavrikakis, M.; Chi, M.; More, K. L.; Li, Y.; Markovic, N. M.; Somorjai, G. A.; Yang, P.; Stamenkovic, V. R. Highly Crystalline Multimetallic Nanoframes with Three-Dimensional Electrocatalytic Surfaces. *Science* **2014**, *343* (6177), 1339–1343. <https://doi.org/10.1126/science.1249061>.
- (16) Stamenkovic, V.; Mun, B. S.; Mayrhofer, K. J. J.; Ross, P. N.; Markovic, N. M.; Rossmeisl, J.; Greeley, J.; Nørskov, J. K. Changing the Activity of Electrocatalysts for Oxygen Reduction by Tuning the Surface Electronic Structure. *Angew. Chem. Int. Ed.* **2006**, *45* (18), 2897–2901. <https://doi.org/10.1002/anie.200504386>.
- (17) Shao, M.; Peles, A.; Shoemaker, K.; Gummalla, M.; Njoki, P. N.; Luo, J.; Zhong, C.-J. Enhanced Oxygen Reduction Activity of Platinum Monolayer on Gold Nanoparticles. *J. Phys. Chem. Lett.* **2011**, *2* (2), 67–72. <https://doi.org/10.1021/jz1015789>.
- (18) Kaito, T.; Mitsumoto, H.; Sugawara, S.; Shinohara, K.; Uehara, H.; Ariga, H.; Takakusagi, S.; Hatakeyama, Y.; Nishikawa, K.; Asakura, K. K-Edge X-Ray Absorption Fine Structure Analysis of Pt/Au Core–Shell Electrocatalyst: Evidence for Short Pt–Pt Distance. *J. Phys. Chem. C* **2014**, *118* (16), 8481–8490. <https://doi.org/10.1021/jp501607f>.
- (19) Shen, L.-L.; Zhang, G.-R.; Miao, S.; Liu, J. (Jimmy); Xu, B.-Q. Core–Shell Nanostructured Au@Ni_mPt₂ Electrocatalysts with Enhanced Activity and Durability for Oxygen Reduction Reaction. *ACS Catal.* **2016**, *6* (3), 1680–1690. <https://doi.org/10.1021/acscatal.5b02124>.
- (20) Du, J.; Quinson, J.; Zana, A.; Arenz, M. Elucidating Pt-Based Nanocomposite Catalysts for the Oxygen Reduction Reaction in Rotating Disk Electrode and Gas Diffusion Electrode Measurements. *ACS Catal.* **2021**, *11* (12), 7584–7594. <https://doi.org/10.1021/acscatal.1c01496>.
- (21) Liu, G.; Shih, A. J.; Deng, H.; Ojha, K.; Chen, X.; Luo, M.; McCrum, I. T.; Koper, M. T. M.; Greeley, J.; Zeng, Z. Site-Specific Reactivity of Stepped Pt Surfaces Driven by Stress Release. *Nature* **2024**, *626* (8001), 1005–1010. <https://doi.org/10.1038/s41586-024-07090-z>.
- (22) Zhang, J.; Sasaki, K.; Sutter, E.; Adzic, R. R. Stabilization of Platinum Oxygen-Reduction Electrocatalysts Using Gold Clusters. *Science* **2007**, *315* (5809), 220–222. <https://doi.org/10.1126/science.1134569>.
- (23) Zhang, Y.; Huang, Q.; Zou, Z.; Yang, J.; Vogel, W.; Yang, H. Enhanced Durability of Au Cluster Decorated Pt Nanoparticles for the Oxygen Reduction Reaction. *J. Phys. Chem. C* **2010**, *114* (14), 6860–6868. <https://doi.org/10.1021/jp100559g>.
- (24) Viswanathan, V.; Hansen, H. A.; Rossmeisl, J.; Nørskov, J. K. Unifying the 2e⁻ and 4e⁻ Reduction of Oxygen on Metal Surfaces. *J. Phys. Chem. Lett.* **2012**, *3* (20), 2948–2951. <https://doi.org/10.1021/jz301476w>.
- (25) Hammer, B.; Norskov, J. K. Why Gold Is the Noblest of All the Metals. *Nature* **1995**, *376* (6537), 238–240. <https://doi.org/10.1038/376238a0>.
- (26) Wanjala, B. N.; Luo, J.; Fang, B.; Mott, D.; Zhong, C.-J. Gold-Platinum Nanoparticles: Alloying and Phase Segregation. *J Mater Chem* **2011**, *21* (12), 4012–4020. <https://doi.org/10.1039/C0JM02682D>.
- (27) Saksena, A.; Chien, Y.-C.; Chang, K.; Kümmerl, P.; Hans, M.; Völker, B.; Schneider,

- J. M. Metastable Phase Formation of Pt-X (X = Ir, Au) Thin Films. *Sci. Rep.* **2018**, *8* (1), 10198. <https://doi.org/10.1038/s41598-018-28452-4>.
- (28) Hernández-Fernández, P.; Rojas, S.; Ocón, P.; Gómez De La Fuente, J. L.; San Fabián, J.; Sanza, J.; Peña, M. A.; García-García, F. J.; Terreros, P.; Fierro, J. L. G. Influence of the Preparation Route of Bimetallic Pt–Au Nanoparticle Electrocatalysts for the Oxygen Reduction Reaction. *J. Phys. Chem. C* **2007**, *111* (7), 2913–2923. <https://doi.org/10.1021/jp066812k>.
- (29) Ma, Y.; Balbuena, P. B. Pt Surface Segregation in Bimetallic Pt3M Alloys: A Density Functional Theory Study. *Surf. Sci.* **2008**, *602* (1), 107–113. <https://doi.org/10.1016/j.susc.2007.09.052>.
- (30) Brimaud, S.; Engstfeld, A. K.; Alves, O. B.; Behm, R. J. Structure–Reactivity Correlation in the Oxygen Reduction Reaction: Activity of Structurally Well Defined Au Pt_{1–x}Pt(111) Monolayer Surface Alloys. *J. Electroanal. Chem.* **2014**, *716*, 71–79. <https://doi.org/10.1016/j.jelechem.2013.10.017>.
- (31) Bergbreiter, A.; Alves, O. B.; Hoster, H. E. Entropy Effects in Atom Distribution and Electrochemical Properties of Au_xPt_{1-x}/Pt(111) Surface Alloys. *ChemPhysChem* **2010**, *11* (7), 1505–1512. <https://doi.org/10.1002/cphc.201000105>.
- (32) Tsong, T. T.; Ng, Y. S.; McLane, S. B. Surface Segregation of a Pt–Au Alloy: An Atom-Probe Field Ion Microscope Investigation. *J. Chem. Phys.* **1980**, *73* (3), 1464–1468. <https://doi.org/10.1063/1.440208>.
- (33) Kuntze, J.; Speller, S.; Heiland, W.; Atrei, A.; Rovida, G.; Bardi, U. Surface Structure and Composition of the Alloy Au 3 Pd (100) Determined by LEED and Ion Scattering Spectroscopy. *Phys. Rev. B* **1999**, *60* (3), 1535–1538. <https://doi.org/10.1103/PhysRevB.60.1535>.
- (34) Kuntze, J.; Speller, S.; Heiland, W.; Deurinck, P.; Creemers, C.; Atrei, A.; Bardi, U. Surface Structure and Segregation Profile of the Alloy Au 3 Pd (110): Experiment and Theory. *Phys. Rev. B* **1999**, *60* (12), 9010–9018. <https://doi.org/10.1103/PhysRevB.60.9010>.
- (35) Schömann, S.; Taglauer, E. SURFACE SEGREGATION ON Au₃Cu (001). *Surf. Rev. Lett.* **1996**, *03* (05n06), 1823–1829. <https://doi.org/10.1142/S0218625X96002758>.
- (36) Beikler, R.; Taglauer, E. Surface Segregation at the Binary Alloy CuAu (100) Studied by Low-Energy Ion Scattering. *Surf. Sci.* **2016**, *643*, 138–141. <https://doi.org/10.1016/j.susc.2015.08.030>.
- (37) Enkovaara, J.; Rostgaard, C.; Mortensen, J. J.; Chen, J.; Dułak, M.; Ferrighi, L.; Gavnholt, J.; Glinsvad, C.; Haikola, V.; Hansen, H. A.; Kristoffersen, H. H.; Kuisma, M.; Larsen, A. H.; Lehtovaara, L.; Ljungberg, M.; Lopez-Acevedo, O.; Moses, P. G.; Ojanen, J.; Olsen, T.; Petzold, V.; Romero, N. A.; Stausholm-Møller, J.; Strange, M.; Tritsaris, G. A.; Vanin, M.; Walter, M.; Hammer, B.; Häkkinen, H.; Madsen, G. K. H.; Nieminen, R. M.; Nørskov, J. K.; Puska, M.; Rantala, T. T.; Schiøtz, J.; Thygesen, K. S.; Jacobsen, K. W. Electronic Structure Calculations with GPAW: A Real-Space Implementation of the Projector Augmented-Wave Method. *J. Phys. Condens. Matter* **2010**, *22* (25), 253202. <https://doi.org/10.1088/0953-8984/22/25/253202>.
- (38) Blöchl, P. E. Projector Augmented-Wave Method. *Phys. Rev. B* **1994**, *50* (24), 17953–17979. <https://doi.org/10.1103/PhysRevB.50.17953>.
- (39) Hjorth Larsen, A.; Jørgen Mortensen, J.; Blomqvist, J.; Castelli, I. E.; Christensen, R.; Dułak, M.; Friis, J.; Groves, M. N.; Hammer, B.; Hargus, C.; Hermes, E. D.; Jennings, P. C.; Bjerre Jensen, P.; Kermode, J.; Kitchin, J. R.; Leonhard Kolsbjerg, E.; Kubal, J.; Kaasbjerg, K.; Lysgaard, S.; Bergmann Maronsson, J.; Maxson, T.; Olsen, T.; Pastewka, L.; Peterson, A.; Rostgaard, C.; Schiøtz, J.; Schütt, O.; Strange, M.; Thygesen, K. S.; Vegge, T.; Vilhelmsen, L.; Walter, M.; Zeng, Z.; Jacobsen, K. W. The Atomic Simulation Environment—a Python Library for Working with Atoms. *J. Phys. Condens. Matter* **2017**, *29* (27), 273002. <https://doi.org/10.1088/1361-648X/aa680e>.
- (40) Hammer, B.; Hansen, L. B.; Nørskov, J. K. Improved Adsorption Energetics within Density-Functional Theory Using Revised Perdew-Burke-Ernzerhof Functionals. *Phys. Rev. B* **1999**, *59* (11), 7413–7421. <https://doi.org/10.1103/PhysRevB.59.7413>.

- (41) Man, I. C.; Su, H.; Calle-Vallejo, F.; Hansen, H. A.; Martínez, J. I.; Inoglu, N. G.; Kitchin, J.; Jaramillo, T. F.; Nørskov, J. K.; Rossmeisl, J. Universality in Oxygen Evolution Electrocatalysis on Oxide Surfaces. *ChemCatChem* **2011**, 3 (7), 1159–1165. <https://doi.org/10.1002/cctc.201000397>.
- (42) Koper, M. T. M. Thermodynamic Theory of Multi-Electron Transfer Reactions: Implications for Electrocatalysis. *J. Electroanal. Chem.* **2011**, 660 (2), 254–260. <https://doi.org/10.1016/j.jelechem.2010.10.004>.
- (43) Christensen, R.; Hansen, H. A.; Dickens, C. F.; Nørskov, J. K.; Vegge, T. Functional Independent Scaling Relation for ORR/OER Catalysts. *J. Phys. Chem. C* **2016**, 120 (43), 24910–24916. <https://doi.org/10.1021/acs.jpcc.6b09141>.
- (44) Bedürftig, K.; Völkening, S.; Wang, Y.; Winterlin, J.; Jacobi, K.; Ertl, G. Vibrational and Structural Properties of OH Adsorbed on Pt(111). *J. Chem. Phys.* **1999**, 111 (24), 11147–11154. <https://doi.org/10.1063/1.480472>.
- (45) Pedersen, J. K.; Batchelor, T. A. A.; Yan, D.; Skjegstad, L. E. J.; Rossmeisl, J. Surface Electrocatalysis on High-Entropy Alloys. *Curr. Opin. Electrochem.* **2021**, 26, 100651. <https://doi.org/10.1016/j.coelec.2020.100651>.
- (46) Beckord, S.; Brimaud, S.; Behm, R. J. The Performance of Structurally Well-Defined Ag_xPt_{1-x}/Pt(111) Surface Alloys in the Oxygen Reduction Reaction – An Atomic-Scale Picture. *J. Electroanal. Chem.* **2018**, 819, 401–409. <https://doi.org/10.1016/j.jelechem.2017.11.038>.
- (47) Stephens, I. E. L.; Bondarenko, A. S.; Perez-Alonso, F. J.; Calle-Vallejo, F.; Bech, L.; Johansson, T. P.; Jepsen, A. K.; Frydendal, R.; Knudsen, B. P.; Rossmeisl, J.; Chorkendorff, I. Tuning the Activity of Pt(111) for Oxygen Electroreduction by Subsurface Alloying. *J. Am. Chem. Soc.* **2011**, 133 (14), 5485–5491. <https://doi.org/10.1021/ja111690g>.
- (48) Sabatier, P. Hydrogénations et Déshydrogénations Par Catalyse. *Berichte Dtsch. Chem. Ges.* **1911**, 44 (3), 1984–2001. <https://doi.org/10.1002/cber.19110440303>.
- (49) Yu, A.; Liu, S.; Yang, Y. Recent Advances in Electrosynthesis of H₂O₂ via Two-Electron Oxygen Reduction Reaction. *Chem. Commun.* **2024**, 60 (40), 5232–5244. <https://doi.org/10.1039/D4CC01476F>.
- (50) Jiang, Y.; Ni, P.; Chen, C.; Lu, Y.; Yang, P.; Kong, B.; Fisher, A.; Wang, X. Selective Electrochemical H₂O₂ Production through Two-Electron Oxygen Electrochemistry. *Adv. Energy Mater.* **2018**, 8 (31), 1801909. <https://doi.org/10.1002/aenm.201801909>.
- (51) Wang, N.; Ma, S.; Zuo, P.; Duan, J.; Hou, B. Recent Progress of Electrochemical Production of Hydrogen Peroxide by Two-Electron Oxygen Reduction Reaction. *Adv. Sci.* **2021**, 8 (15), 2100076. <https://doi.org/10.1002/advs.202100076>.
- (52) Siahrostami, S.; Verdaguer-Casadevall, A.; Karamad, M.; Deiana, D.; Malacrida, P.; Wickman, B.; Escudero-Escribano, M.; Paoli, E. A.; Frydendal, R.; Hansen, T. W.; Chorkendorff, I.; Stephens, I. E. L.; Rossmeisl, J. Enabling Direct H₂O₂ Production through Rational Electrocatalyst Design. *Nat. Mater.* **2013**, 12 (12), 1137–1143. <https://doi.org/10.1038/nmat3795>.
- (53) Blanco-Redondo, L.; Lobko, Y.; Veltruská, K.; Nováková, J.; Mazur, M.; Darabut, A. M.; Hrbek, T.; Dopita, M.; Hraníček, J.; Yakovlev, Y.; Matolínová, I.; Matolín, V. Bifunctional Pt–Ir Nanoparticle Catalysts for Oxygen Reduction and Evolution Reactions: Investigating the Influence of Surface Composition on the Catalytic Properties. *Sustain. Energy Fuels* **2024**, 8 (4), 797–810. <https://doi.org/10.1039/D3SE01238G>.
- (54) Stamenković, V.; Schmidt, T. J.; Ross, P. N.; Marković, N. M. Surface Composition Effects in Electrocatalysis: Kinetics of Oxygen Reduction on Well-Defined Pt₃Ni and Pt₃Co Alloy Surfaces. *J. Phys. Chem. B* **2002**, 106 (46), 11970–11979. <https://doi.org/10.1021/jp021182h>.
- (55) Stamenkovic, V. R.; Mun, B. S.; Mayrhofer, K. J. J.; Ross, P. N.; Markovic, N. M. Effect of Surface Composition on Electronic Structure, Stability, and Electrocatalytic Properties of Pt-Transition Metal Alloys: Pt-Skin versus Pt-Skeleton Surfaces. *J. Am. Chem. Soc.* **2006**, 128 (27), 8813–8819. <https://doi.org/10.1021/ja0600476>.
- (56) Komanicky, V.; Iddir, H.; Chang, K.-C.; Menzel, A.; Karapetrov, G.; Hennessy, D.;

- Zapol, P.; You, H. Shape-Dependent Activity of Platinum Array Catalyst. *J. Am. Chem. Soc.* **2009**, 131 (16), 5732–5733. <https://doi.org/10.1021/ja900459w>.
- (57) Cao, S.; Tao, F. (Feng); Tang, Y.; Li, Y.; Yu, J. Size- and Shape-Dependent Catalytic Performances of Oxidation and Reduction Reactions on Nanocatalysts. *Chem. Soc. Rev.* **2016**, 45 (17), 4747–4765. <https://doi.org/10.1039/C6CS00094K>.
- (58) Wang, Y.-J.; Zhao, N.; Fang, B.; Li, H.; Bi, X. T.; Wang, H. Carbon-Supported Pt-Based Alloy Electrocatalysts for the Oxygen Reduction Reaction in Polymer Electrolyte Membrane Fuel Cells: Particle Size, Shape, and Composition Manipulation and Their Impact to Activity. *Chem. Rev.* **2015**, 115 (9), 3433–3467. <https://doi.org/10.1021/cr500519c>.
- (59) Polani, S.; MacArthur, K. E.; Klingenhof, M.; Wang, X.; Paciok, P.; Pan, L.; Feng, Q.; Kormányos, A.; Cherevko, S.; Heggen, M.; Strasser, P. Size and Composition Dependence of Oxygen Reduction Reaction Catalytic Activities of Mo-Doped PtNi/C Octahedral Nanocrystals. *ACS Catal.* **2021**, 11 (18), 11407–11415. <https://doi.org/10.1021/acscatal.1c01761>.
- (60) Gan, L.; Rudi, S.; Cui, C.; Heggen, M.; Strasser, P. Size-Controlled Synthesis of Sub-10 Nm PtNi₃ Alloy Nanoparticles and Their Unusual Volcano-Shaped Size Effect on ORR Electrocatalysis. *Small* **2016**, 12 (23), 3189–3196. <https://doi.org/10.1002/smll.201600027>.
- (61) Koenigsmann, C.; Sutter, E.; Adzic, R. R.; Wong, S. S. Size- and Composition-Dependent Enhancement of Electrocatalytic Oxygen Reduction Performance in Ultrathin Palladium–Gold (Pd_{1-x}Au_x) Nanowires. *J. Phys. Chem. C* **2012**, 116 (29), 15297–15306. <https://doi.org/10.1021/jp306034d>.
- (62) Lopes, P. P.; Li, D.; Lv, H.; Wang, C.; Tripkovic, D.; Zhu, Y.; Schimmenti, R.; Daimon, H.; Kang, Y.; Snyder, J.; Becknell, N.; More, K. L.; Strmcnik, D.; Markovic, N. M.; Mavrikakis, M.; Stamenkovic, V. R. Eliminating Dissolution of Platinum-Based Electrocatalysts at the Atomic Scale. *Nat. Mater.* **2020**, 19 (11), 1207–1214. <https://doi.org/10.1038/s41563-020-0735-3>.
- (63) Xie, X.; Briega-Martos, V.; Farris, R.; Dopita, M.; Vorokhta, M.; Skála, T.; Matolínová, I.; Neyman, K. M.; Cherevko, S.; Khalakhan, I. Optimal Pt–Au Alloying for Efficient and Stable Oxygen Reduction Reaction Catalysts. *ACS Appl. Mater. Interfaces* **2023**, 15 (1), 1192–1200. <https://doi.org/10.1021/acsami.2c18655>.
- (64) Davey, W. P. Precision Measurements of the Lattice Constants of Twelve Common Metals. *Phys. Rev.* **1925**, 25 (6), 753–761. <https://doi.org/10.1103/PhysRev.25.753>.